16 Jun 2022

Complex Rupture and Triggered Aseismic Creep during the 14 August 2021 Haiti Earthquake from Satellite Geodesy

Jeremy Maurer
Missouri University of Science and Technology, jlmd9g@mst.edu

R. Dutta

A. Vernon

S. Vajedian

Recommended Citation

J. Maurer et al., "Complex Rupture and Triggered Aseismic Creep during the 14 August 2021 Haiti Earthquake from Satellite Geodesy," *Geophysical Research Letters*, vol. 49, no. 11, article no. e2022GL098573, Wiley; American Geophysical Union, Jun 2022.
The definitive version is available at https://doi.org/10.1029/2022GL098573

AGU ADVANCING EARTH AND SPACE SCIENCE

Geophysical Research Letters®

RESEARCH LETTER
10.1029/2022GL098573

Key Points:

- The 2021 Haiti earthquake ruptured the Enriquillo-Plantain Garden Fault as thrust slip east of Pic Macaya and left-lateral slip to the west
- Slip occurred on multiple fault segments and jumped across the restraining bend at Pic Macaya
- InSAR observations indicate afterslip in the 4 days following the event of a similar magnitude to the coseismic slip

Supporting Information:

Supporting Information may be found in the online version of this article.

Correspondence to:

J. Maurer,
jmaurer@mst.edu

Citation:

Maurer, J., Dutta, R., Vernon, A., & Vajedian, S. (2022). Complex rupture and triggered aseismic creep during the 14 August 2021 Haiti earthquake from satellite geodesy. *Geophysical Research Letters*, *49*, e2022GL098573. https://doi.org/10.1029/2022GL098573

Received 3 MAR 2022
Accepted 25 MAY 2022

Author Contributions:

Conceptualization: J. Maurer, R. Dutta, S. Vajedian
Data curation: J. Maurer, A. Vernon
Formal analysis: J. Maurer, R. Dutta, A. Vernon
Investigation: R. Dutta
Methodology: J. Maurer, R. Dutta, A. Vernon, S. Vajedian
Software: J. Maurer, R. Dutta
Validation: J. Maurer, R. Dutta
Visualization: J. Maurer
Writing – original draft: J. Maurer, R. Dutta
Writing – review & editing: J. Maurer, R. Dutta, S. Vajedian

Complex Rupture and Triggered Aseismic Creep During the 14 August 2021 Haiti Earthquake From Satellite Geodesy

J. Maurer[1], R. Dutta[1], A. Vernon[1], and S. Vajedian[1]

[1]Geological Sciences and Geological and Petroleum Engineering, Missouri University of Science and Technology, Rolla, MO, USA

Abstract The 2021 August 14 M_W 7.2 Nippes, Haiti earthquake occurred 75 km west of the epicenter of the 2010 Leogane earthquake (Haiti) on the transpressive Caribbean - North America plate boundary. We present an updated fault map for Hispaniola and model coseismic and early postseismic fault slip using Interferometric Synthetic Aperture Radar and pixel offsets. We find the earthquake ruptured multiple segments of the Enriquillo-Plantain Garden Fault Zone. Slip occurred in two main sub-events on either side of a restraining bend at Pic Macaya, with ~2.7 m of peak reverse-slip east of the bend. To the west, slip jumps the restraining bend and further ruptures with ~1.2 m of left-lateral slip. Afterslip in the 4 days following the event occurred at shallow depth and adjacent to the coseismic rupture areas and reached the surface east of Pic Macaya.

Plain Language Summary On 14 August 2021, a large M_W7.2 earthquake struck southwestern Haiti, 75 km to the west of the 2010 Leogane, Haiti earthquake. We use remotely-sensed data from two Synthetic Aperture Radar missions, ALOS-2 and Sentinel-1, and a new fault map database to study the earthquake and try to determine which faults slipped and where, and how much. We built a model of fault slip during the earthquake and aseismic slip that followed the earthquake, called afterslip. By comparing our results with previously published results using seismic data, we suggest that the earthquake started out with reverse slip on the Enriquillo-Plantain Garden Fault Zone (EPGFZ) near the hypocenter. It then jumped the restraining bend in the EPGFZ near Pic Macaya, and ruptured west of the restraining bend with left-lateral slip. The earthquake appears to be very complex and ruptured multiple faults. Afterslip in the 4 days following the earthquake was nearly as large as the earthquake, reaching the surface after ~3 days. Taken together, the modeling results paint a picture of a complex fault system with highly variable stress and stability.

1. Introduction

The 14 August 2021 M_W7.2 Nippes earthquake struck the Tiburon peninsula in southwest Haiti and affected 800,000 people, caused over 2,000 deaths, and resulted in 1.6 billion USD in economic losses (UN-OCHA, 2021). The earthquake occurred just 11.5 years after the devastating M_w7.0 2010 earthquake that happened near Port-au-Prince, Haiti (Figure 1), and left a 75-km seismic gap between the two events. Haiti occupies the western third of the island of Hispaniola within the Gonave microplate on the boundary between the converging Caribbean (CA) and North American (NA) plates (Benford et al., 2012; Mann et al., 1995). Based on the USGS moment tensor solution (Figure 1), the Nippes earthquake was an oblique left-lateral thrust event that occurred on or near the Enriquillo-Plantain Garden Fault Zone (EPGFZ), a major plate-bounding strike-slip fault in the Tiburon peninsula (Figure S1 in Supporting Information S1). The EPGFZ is a well-expressed major fault system that is thought to have ruptured in major historic earthquakes (e.g., Bakun et al., 2012; Prentice et al., 2010) and accommodates a large fraction of the 19 mm/yr N73E Caribbean - North America relative plate motion (Benford et al., 2012; Calais et al., 2016; DeMets et al., 2010; Mann et al., 2002; Symithe et al., 2015). The EPGFZ is the eastward extension of the Walton fault east of Jamaica and may merge with the Muertos Trough offshore southern Hispaniola (DeMets & Wiggins-Grandison, 2007; Leroy et al., 2015) or die out (Saint Fleur et al., 2020). Faults on the Tiburon peninsula accommodate both strike-slip and compressional motion (Benford et al., 2012; Corbeau, Rolandone, Leroy, Meyer, et al., 2016; Symithe and Calais, 2016), but the EPGFZ itself has been traditionally considered to be primarily a strike-slip fault with a dip near vertical (e.g., Douilly et al., 2013; Mann et al., 1995; Prentice et al., 2010; Saint Fleur et al., 2015; Symithe et al., 2013).

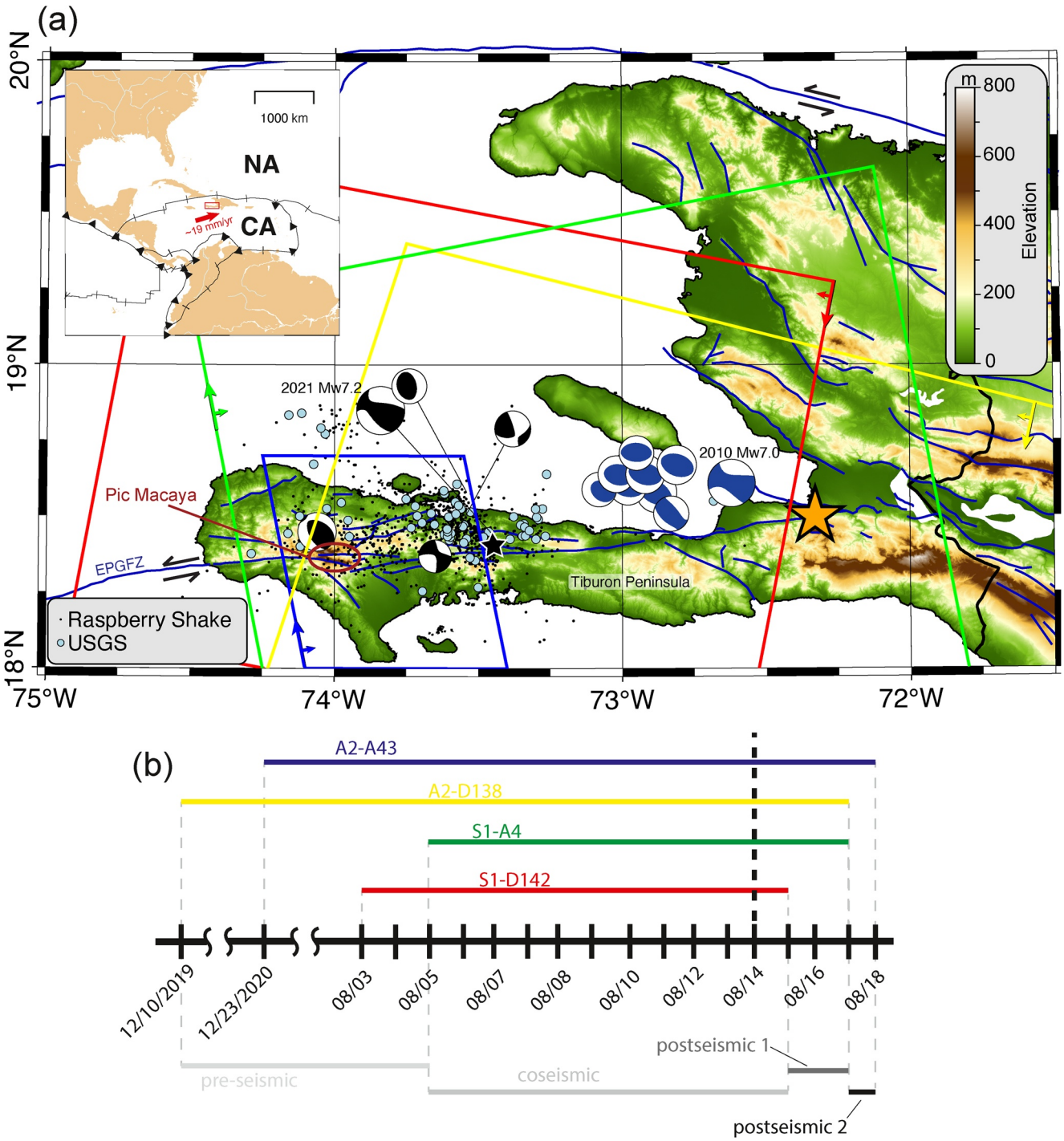

Figure 1. (a) Seismotectonic context and Interferometric Synthetic Aperture Radar (InSAR) footprints for the August 2021 Mw7.2 Haiti earthquake (black star is the epicenter location). Black beachballs are Centroid Moment Tensors (CMTs; Dziewonski et al., 1981; Ekström et al., 2012) for the M_W7.2 mainshock and large aftershocks through 31 January 2022. The location of the 2010 earthquake and large aftershocks are also shown with the blue CMTs. Gray dots are earthquake locations from COMCAT and black dots are from the Raspberry Shake citizen-seismometer network, both including data from 13 August 2021–31 January 2022 (see Data and Resources). Blue lines are the updated faults (Supp. Text S1). Colored polygons are InSAR data footprints: Sentinel-1 descending track 142 (red), Sentinel-1 ascending track 4 (green), ALOS-2 ascending track 43 (blue), and ALOS-2 descending track 138 (yellow). Orange star is Port-au-Prince. Inset shows the Caribbean (CA) plate motion relative to the North American (NA) plate. See Data and Resources for details on the digital elevation model and plotting software. (b) Temporal footprints of the InSAR observations and corresponding separable slip phases. The time of the earthquake is shown as a vertical dashed line. The phases given beneath the timeline ("pre-seismic," "coseismic," etc.) represent the different time periods we model separately in the inversion (see Section 2.3).

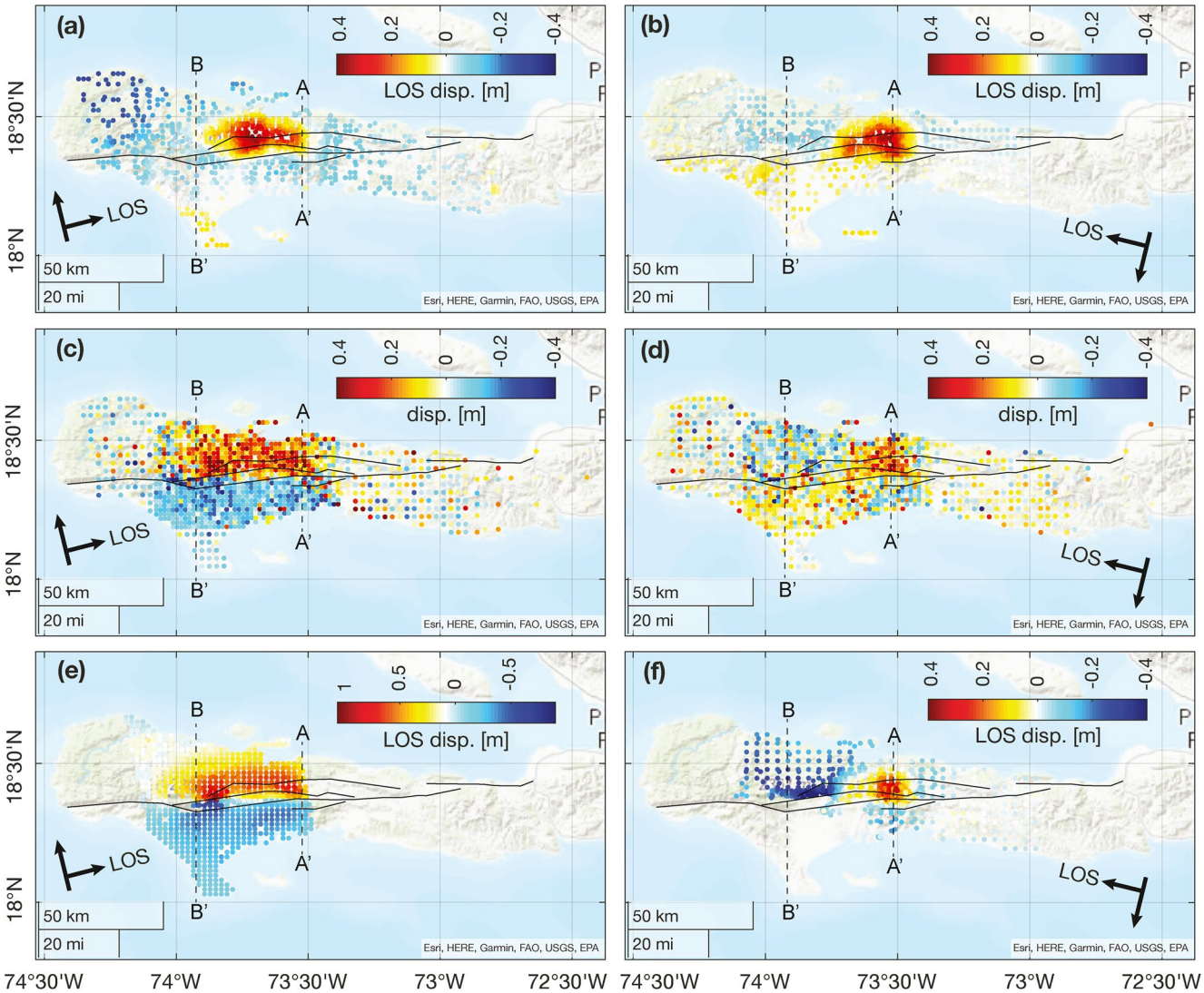

Figure 2. Downsampled Interferometric Synthetic Aperture Radar (InSAR) and pixel offset displacements from Sentinel-1 and ALOS-2 used to estimate slip on the fault system. Positive motion is toward the satellite. (a and b) Sentinel-1 InSAR, (c and d) Sentinel-1 range pixel offsets, (e and f) ALOS-2 InSAR. (a,c,e) are the ascending data (S1 track 4, A2 track 43). (b, d, and f) are the descending data (S1 track 142, A2 track 138). Data along the profiles A-A' and B-B' are shown in Figure 4. Acquisition dates are shown in Figure 1b and Tables S1 and S2 in Supporting Information S1, and the full-resolution data is shown in Figure S4 of Supporting Information S1.

Similar to the 2010 earthquake, the Nippes earthquake appears to be complex and involve both reverse and left-lateral slip. Okuwaki and Fan (2022) used teleseismic finite-fault inversion and P-wave back-projection and found that the earthquake ruptured two separate regions of southwest Haiti, first near the event hypocenter with primarily reverse faulting, and the other west of the restraining bend at Pic Macaya (Figure 1a) with primarily left-lateral faulting. They argue that neither sub-event occurred on the EPGFZ but on different nearby faults. However, the dip-angle and geometry of the EPGFZ are not well known. The earthquake left a 75-km seismic gap between the location of the 2010 and 2021 events, with no large aftershocks in the gap region after either earthquake (Figure 1a). Instead, aftershocks of the 2010 earthquake followed a thrust fault offshore, while aftershocks of the 2021 earthquake were mostly around the mainshock location.

In this study, we analyze Synthetic Aperture Radar (SAR) data from Copernicus Sentinel-1 and Interferometric SAR (InSAR) images from Sentinel-1 and the Japan Aerospace Exploration Agency (JAXA) Advanced Land Observation Satellite-2 (ALOS-2) satellites (Figures 1 and 2). We present a new fault database for the Tiburon peninsula and use it to generate potential fault geometries for the EPGFZ and nearby faults. We use the

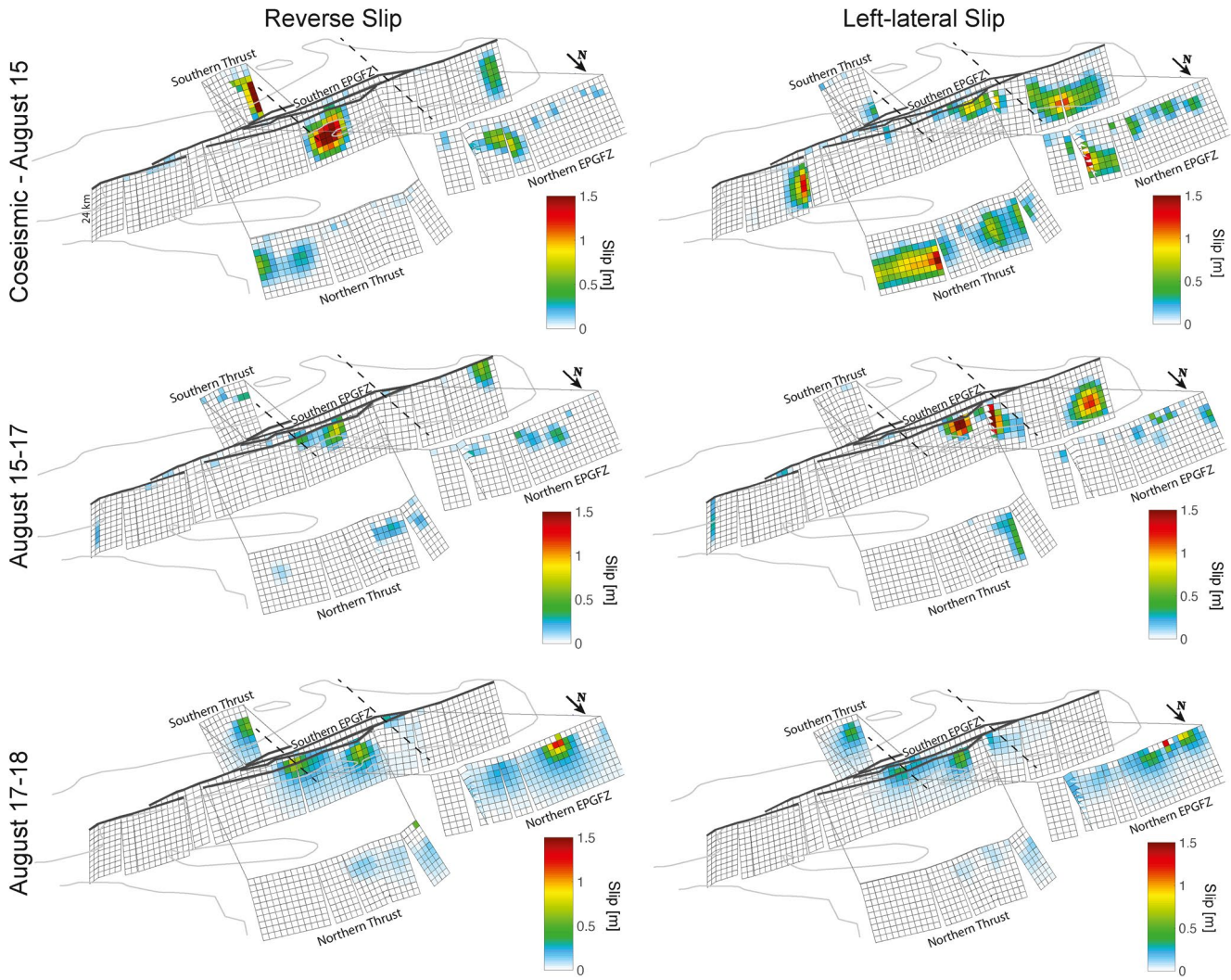

Figure 3. Modeled slip during the different phases. The fault system has been exploded and rotated to view from the northeast to aid visualization. Dashed black lines are the same profile lines as in Figure 2.

observations to develop models of coseismic fault slip and afterslip through 4 days after the event and compare them with the seismic-only results of Okuwaki and Fan (2022) and regional topography.

2. Data and Methods

2.1. Updated Fault Map Database for Southern Haiti

We developed a new fault map database through compiling and comparing several sources for fault geometry in Hispaniola (Maurer & Vernon, 2022; Figure 1). We added to an existing database for the region, the Caribbean and Central American active fault database (CCAF-DB; Styron et al., 2020). We incorporated additional data sources (Conrad et al., 2020; Corbeau, Rolandone, Leroy, Mercier de Lépinay, et al., 2016; French & Schenk, 2004; Possee et al., 2019; Saint Fleur et al., 2020) and compared to Shuttle Radar Topography Mission digital elevation model (SRTM) and Light Detection And Ranging (LiDAR) DEMs. We used the updated fault traces database to build a 3D fault model for the earthquake, including southern and northern branches of the EPGFZ, a thrust fault south of the epicentral location, and a larger northern thrust fault (Figures 1 and 3 and Figures S2 and S3 in Supporting Information S1).

2.2. SAR Observations

We used surface displacements derived from four different SAR geometries (Figures 1 and 2, Figures S4 and S5 in Supporting Information S1). We obtained single-look complex (SLC) SAR images from two Sentinel-1A/B tracks (C-band, ∼5.6 cm wavelength), acquired in Terrain Observations with Progressive Scans in azimuth mode. The SLC images were processed with the InSAR Scientific Computing Environment (ISCE) v.2 software (Rosen et al., 2012) "topsApp.py" application. For each track, the secondary radar scenes are geometrically aligned (coregistered) to the reference scene using the Enhanced Spectral Diversity method (ESD; Fattahi et al., 2017). We observed no residual along-track shifts in InSAR with this method. Precise orbit ephemeris data was used to remove orbital contributions from the interferometric phase. We performed regular interferometric processing to make interferograms and coherence maps. The interferograms were corrected for topography-related phase components using the 30 m resolution SRTM DEM (Farr et al., 2007), filtered using Goldstein-Werner adaptive filtering (Goldstein & Werner, 1998) and unwrapped using the statistical Minimum Cost Flow algorithm (Chen & Zebker, 2001, 2002). To produce SAR range pixel offsets, amplitude images were cross-correlated using a matching window of 64 pixels in range and 16 pixels in azimuth. The amplitude images are oversampled by a factor of 64 to obtain 1/64 of a pixel precision. We applied a 500 m median filter to reduce noise.

The ALOS-2 PALSAR-2 L-band (22.9 cm wavelength) interferograms were provided by the JAXA and were already fully processed and low-quality pixels masked, so we used these products as provided. We removed disconnected areas away from the main rupture area, especially for descending track (orbit 138). Further details of each data set are given in Supp. Tables S1–S2 in Supporting Information S1.

We downsampled the interferograms using a quadtree technique (Jónsson et al., 2002) and the pixel offsets with a 3 km median filter. To account for spatially-correlated errors, we estimate variograms and compute full covariance matrices for the observations using data located away from the rupture area (Figures S6 and S7 in Supporting Information S1). Some ALOS-2 track 43 displacements show detailed step-overs in fault geometry that are not captured by our model, so we masked out the displacements in the very close vicinity of these stepovers (Figure 2; Figure S8 in Supporting Information S1).

We estimate troposphere corrections using the RAiDER package (see Data and Resources) using the ECMWF ERA-5 weather model (see Data and Resources) and corrected the Sentinel-1 interferograms (e.g., Bekaert et al., 2015; Doin et al., 2009; Jolivet et al., 2011). The corrections did not improve the ALOS-2 interferograms (no RMS reduction). We also removed a plane from each InSAR track in the modeling step to account for ionospheric noise.

Visual inspection of the observations show motion toward the satellite (positive) north of the fault just west of 73.5°W in all tracks. Around 74°W the ascending data is positive while descending data show negative displacements, implying left-lateral slip. The ascending data in particular shows surface rupture near 74°W (Figure 2, Figures S4c, S4e, and S8 in Supporting Information S1). Taken together, these observations imply that the earthquake ruptured as primarily blind reverse-slip in the east and transitioned to primarily left-lateral slip in the west.

2.3. Modeling Approach

The InSAR observations cover different time periods (Figure 1b; Tables S1 and S2 in Supporting Information S1) meaning that they are sensitive to different phases of displacement (Ragon et al., 2019). From Figure 2, the observations are not all consistent, suggesting that afterslip occurred during the 4 days following the mainshock. The first SAR acquisition after the earthquake was Sentinel-1 track 142 on August 15th. We refer to all displacements prior to this time as the "coseismic" period, although it may include early postseismic slip up to the acquisition time (about 22 hr after the earthquake). We assume preseismic deformation in the ALOS-2 data is zero because the interseismic slip rate on the EPGFZ is estimated to be ∼1 cm/yr or less (e.g., Saint Fleur et al., 2020; Symithe & Calais, 2016; Symithe et al., 2015); pre-event displacements are thus negligible compared to coseismic observations (residual 1-sigma of 3.8 cm for D138 and 5.5 cm for A43). We solve for slip during the "coseismic," early postseismic (August 15–17) and later postseismic (August 17–18) time periods.

We constructed a "sheets in the wind" fault model for the Tiburon peninsula around the area of the Haiti earthquake. All fault segments were specified to extend from the surface for a width of 24 km and discretized into square patches. We used 10 patches in the down-dip direction, for a patch size of ∼2.4 × 2.4 km (Figure S3

in Supporting Information S1). We generated Green's functions for a uniform elastic half-space using the Okada (1985) algorithm. In all the models tested, fault dip on the EPGFZ transitions to vertical in the east (Figure 3); this is not required or constrained by the observations but is consistent with prior studies of the EPGFZ (e.g., Possee et al., 2019; Saint Fleur et al., 2015). Figures S9-S15 in Supporting Information S1 show slip and data residuals for several different fault geometries, including a single fault trace, south-dipping, vertical, and several north-dipping angles.

We used bounded linear least-squares to solve for slip on the fault using the interior-point algorithm (*lsqlin* in Matlab). Rather than specifying the rake-angle, we solve for both the dip-slip and strike-slip separately, setting bounds on both slip between 0 and 5 m. This restricts the slip to only be left-lateral and/or reverse (Figure S16 in Supporting Information S1). We used minimum-norm and Laplacian spatial smoothing norm on the slip to regularize the model and constructed a trade-off curve to determine an appropriate choice for the hyperparameters, which scale the two regularization constraints (Figure S17 in Supporting Information S1). Representative cases with rougher and smoother slip models are shown in the Supplement (Figures S18 and S19 and Tables S3 and S4 in Supporting Information S1). Checkerboard tests show how well the datasets resolve slip on the fault in the different time periods (Figure S20 in Supporting Information S1). The goal of the checkerboard tests is to try to determine what type of solutions the inversion produces for a given type of input slip model (i.e., a checkerboard). In our case, we produce solutions that are like the checkerboard for the coseismic and first postseismic periods, but slightly smeared, especially at the extreme ends of the fault. The checkerboard slip pattern in the second postseismic phase is not well resolved, as expected, so we impose a stronger smoothness constraint for that phase. In our modeling, we ignore any contributions from other postseismic displacement mechanisms (e.g., poroelastic relaxation of the crust and viscoelastic relaxation of the lower crust and mantle). Simulations we conducted of poroelastic deformation following the earthquake showed maximum cumulative displacements of less than 1 cm.

3. Results

Testing multiple models for fault geometry shows that the InSAR observations require that the EPGFZ itself be dipping to the north in this area. Tables S3 and S4 in Supporting Information S1 show the misfit and total moment associated with alternative geometries. The preferred model, which assumes two sub-parallel strands of the EPGFZ (southern and northern) dipping at 51° to the north, is the most consistent with both the InSAR observations and Centroid Moment Tensors (CMT) (reduced χ^2 of 2.1). Fault dip of 40 or 70° to the north fit the observations slightly worse than the preferred model, while both vertical (no reverse slip) and south-dipping fault geometry (allowing reverse slip) does not fit the observations (Table S4 and S5 in Supporting Information S1). To further verify the fault dip, we conducted a 2D plane-strain inversion in the epicenter area and used Markov Chain Monte Carlo sampling to determine a uniform slip and fault dip for a north-south profile across the fault near the hypocenter (Text S2 and Figure S21 in Supporting Information S1). The best-fitting fault dip was 52°, consistent with our 3D experiments.

A representative fault slip model is shown in Figure 3; depth profiles of slip are shown in Figure S22 of Supporting Information S1. During the coseismic phase, and consistent with Okuwaki and Fan (2022), slip occurs in two distinct areas over an 80 km-long region. Slip east of Pic Macaya occurred on all three fault branches, with primarily thrust slip on the southern EPGFZ near the hypocenter. Peak thrust slip was ∼2.7 m at a depth of ∼7 km (10 km down-dip). Left-lateral slip occurred from 5 to 10 km depth between the thrust area and Pic Macaya, and 8–22 km depth to the west of Pic Macaya (Figure 1), with peak slip in the west estimated to be 1.2 m at a depth of ∼8 km (12 km down-dip). The easternmost end of the northern thrust fault in the model has a region of high left-lateral slip during the coseismic phase, which is a consistent feature of all the modeling cases (see examples in Figures S9, S10,and S19 of Supporting Information S1), with peak slip ∼1.5 m at a depth of ∼7 km. From the geodetic observations alone, we cannot say whether this eastern slip would have been seismic or aseismic; further detailed analysis including seismic data is required. Predicted 3D displacements from the model in Figure 3 are shown in Figure S23 of Supporting Information S1.

Slip during the first postseismic phase (August 15–17) occurs near the edges of coseismic rupture areas. Reverse slip occurs at ∼3 km depth just up-dip of the coseismic rupture, with peak slip estimated to be ∼1.7 m. Left-lateral slip occurs at the upper-western edge of the mainshock location (∼3 km deep, peak slip ∼2.2 m), which coincides with the location of a left-lateral M_W4.9 aftershock that occurred on August 15 (Figure 1a). About 2.8 m peak

left-lateral slip also occurs within the restraining bend. Finally, ~1.2 m peak left-lateral slip occurs at ~7 km depth on the far western end of the fault. Slip is mostly absent from the other faults in the system during the first postseismic phase. Total moment over the whole fault system during the early postseismic phase is estimated to be M_w6.8, including the M_w4.9 aftershock.

Slip during the second postseismic phase is not well constrained, due to only a single interferogram covering that time period (ALOS-2 track 43). However, some slip is required to fit the observations. Slip occurs on the southern and northern EPGFZ near the surface, and reaches the surface on the northern EPGFZ at the location of the B-B' profile (Figure 2; Figure 4). Total moment during the second postseismic phase is estimated at ~M_w6.8 but is uncertain due to the strong damping and poor resolution (Figure S20 in Supporting Information S1).

4. Discussion

Our preferred model is consistent with Okuwaki and Fan (2022), but in contrast to their study, we find that the data are best explained if both the thrust and left-lateral components of fault slip occurred on the EPGFZ itself. Okuwaki and Fan (2022) show that the rupture began as primarily a reverse-slip event east of the restraining bend and ruptured west, nearly died out in the bend itself (Figure 3 and Okuwaki and Fan, 2002, their Figures 2 and 3) and then revived west of the bend as a left-lateral rupture; thus, the rupture appears to have "jumped" the restraining bend rather than rupturing through, suggesting that it may have been a dynamically triggered phase of rupture. Our results (Figure 3) suggest that aseismic slip may have occurred in the restraining bend gap as afterslip in the first postseismic phase.

The coseismic moment release in all models (including different fault geometries) was lower than the seismically-estimated moment magnitude. This is likely due to a combination of factors. We ignore topography in our modeling, which results in systematically under-estimating the slip (e.g., McTigue & Segall, 1988; Wang & Fialko, 2018) in areas of steep topography around the rupture. Lower slip might have been preferred using the minimum-norm regularization. Steeper fault dip used in other inversion scenarios resulted in slightly higher moments of 7.1–7.2, albeit with worse fit to the data. The inclusion of multiple fault strands results in better overall fit to the data and higher moment and is required to explain the step-over in deformation that is visible in the InSAR observations (see Figure 2 and Figures S4, especially subplot (e), and S8 in Supporting Information S1). Slip on the northernmost thrust fault is uncertain but consistent with the location of aftershocks (Figure 1; Calais et al., 2022). Further work is needed utilizing seismic data to separate seismic and aseismic moment during the coseismic and early postseismic periods.

Slip during the second postseismic phase is not well constrained. Profiles through two areas east of the restraining bend (Figure 4) show that ALOS-2 track 43 has larger displacements than the Sentinel-1 InSAR and pixel offsets and ALOS-2 track 138 InSAR displacements, indicating that a phase of late triggered slip occurred on the fault. This late slip, shown in Figure 3 during the second postseismic phase, involved slip only on the EPFGZ east of Pic Macaya. Displacements in Figure 4c also indicate that afterslip reached the surface after the first postseismic phase.

The amount of postseismic slip estimated to occur during the 4 days after the earthquake is ~86% of the coseismic moment in the model shown in Figure 3, which is large compared to most crustal earthquakes but not outside the range of observed values (Wimpenny et al., 2017). This potentially suggests that high pore pressure or spatial variations in fault frictional properties and/or normal stress could be present on these faults, promoting stable slip in these areas. Further geophysical and modeling work is needed to address which of these possible causes could be responsible for the large afterslip following the earthquake.

Strike-slip motion on the EGPFZ alone cannot fully explain the high topography in the region. Pic Macaya has the highest topography in southwest Haiti at ~1,800 m above sea level and is consistent with push-up tectonics at the restraining bend, while to the east near the hypocenter, a broad region of high elevation (750–1,050 m) is consistent with the location of peak coseismic uplift associated with reverse slip on the EPGFZ (Figure S23 in Supporting Information S1). Although other nearby faults likely accommodate compressional stresses in the region (e.g., during the 2010 Leogane, Haiti earthquake) the current study suggests that some fraction of regional compression is accommodated by the EPGFZ itself. If this is the case, then long-term slip estimated for left-lateral motion (e.g., Saint Fleur et al., 2020) on the EGPFZ is only a part of the total deformation accommodated by the system.

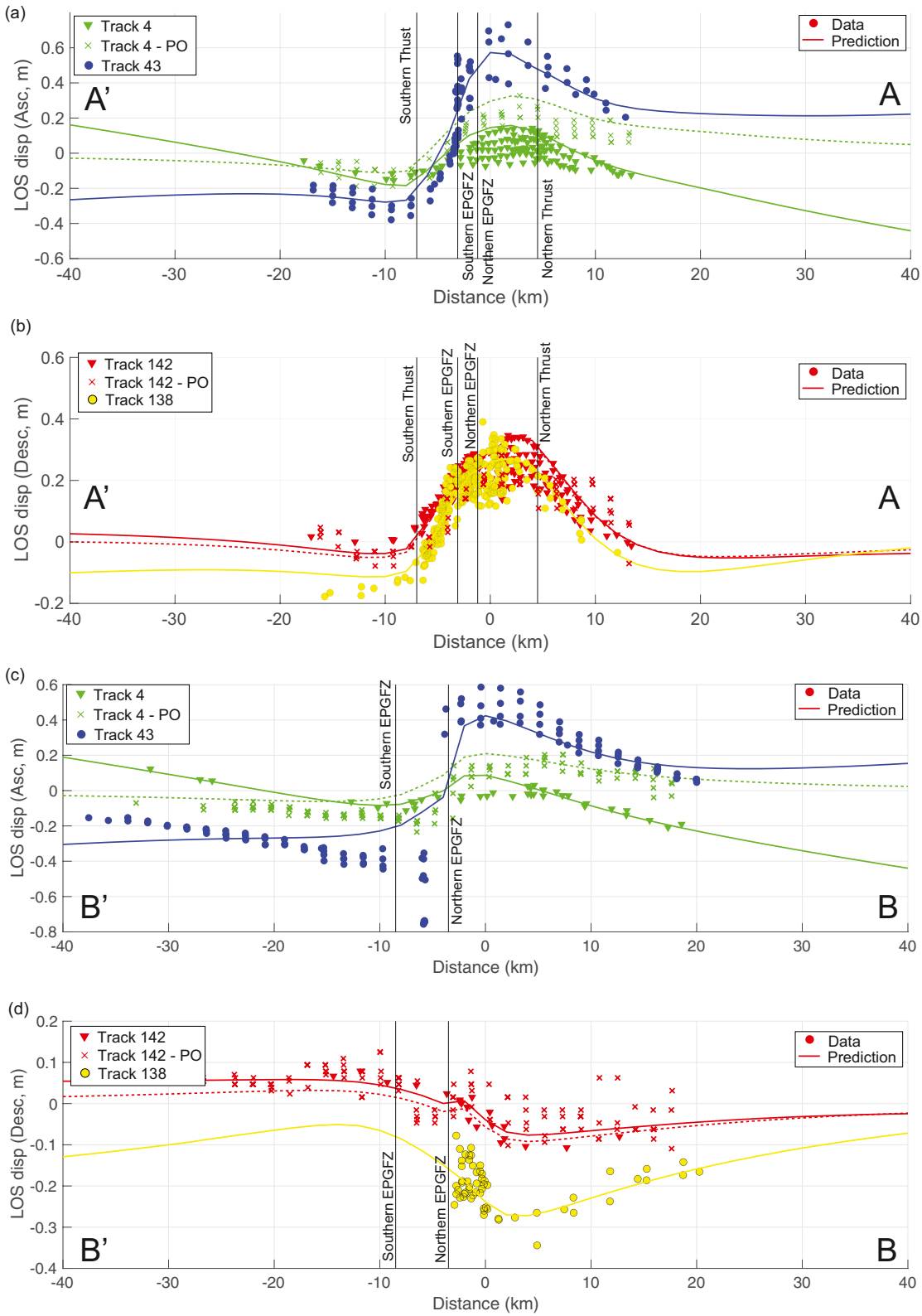

Figure 4. Observed and predicted displacement profiles for the profiles shown in Figure 2. Dashed lines are predicted pixel offsets. (a and b) A-A' profiles; (a) are the ascending observations and (b) are the descending. (c and d) B-B' profiles. (c) Are the ascending observations and (d) are the descending.

5. Conclusions

We present a new fault surface trace map of Hispaniola and use it with multiple InSAR observations to develop a fault slip model for the 2021 Nippes, Haiti earthquake. The earthquake ruptured ~80 km of the EPGFZ in two main sub-events on either side of a restraining bend at Pic Macaya. About 2.7 m of reverse-slip east of the bend near the hypocenter transitioned to left-lateral slip and jumped the restraining bend at Pic Macaya, rupturing the western EPGFZ with about 1.2 m of left-lateral slip. Estimated coseismic moment magnitude is ~M_W7.1. Afterslip in the 4 days following the event reached ~M_W7.0, and occurred up-dip and along-strike of the coseismic rupture areas east of Pic Macaya, breaching the surface west of the main reverse faulting area on August 17th or 18th. The analysis suggests that the EPGFZ accommodates both left-lateral slip and compression, and that multiple fault strands can be active in large earthquakes in the region.

Conflict of Interest

The authors declare no conflicts of interest relevant to this study.

Data Availability Statement

Data and software for replicating the results presented in this study are archived at Maurer (2022). The updated fault database can be found in Maurer and Vernon (2022). We used the UNAVCO plate motion calculator (https://www.unavco.org/software/geodetic-utilities/plate-motion-calculator/plate-motion-calculator.html; last accessed 24 November 2021) to determine the relative motion of the CA plate relative to the NA plate. LiDAR data was retrieved from https://opentopography.org/blog/haiti-lidar-imagery-google-earth, last accessed 14 January 2022. Shuttle Radar Topography Mission (SRTM) 1 Arc-Second Global data was retrieved from https://doi.org/10.5066/F7K072R7, last accessed 14 January 2022. ALOS-2 interferograms were provided by Japan Aerospace Exploration Agency (JAXA) and the Geospatial Information Authority in Japan. Sentinel-1 data were provided by the European Space Agency. Centroid Moment Tensors were obtained from the Global CMT web page. Some figures were created with PyGMT (https://www.pygmt.org/latest/, Uieda et al., 2021). ISCE2 (https://github.com/isce-framework/isce2) was used for processing interferograms. RAiDER (https://github.com/dbekaert/RAiDER) was used to calculate tropospheric noise. The data is published under a Creative Commons Attribution 4.0 International (CC BY 4.0) (see https://creativecommons.org/licenses/by/4.0/).

Acknowledgments

We thank Dezheng Zhao, one anonymous reviewer, and the associate editor for their constructive comments that substantially improved the manuscript. We thank Dr. Jonathan Obrist-Farner and Yi-Chieh Lee for helpful discussions on this topic. We thank Japan Aerospace Exploration Agency (JAXA) and the Geospatial Information Authority of Japan for making the ALOS-2 interferograms freely available. We thank ESA for making access to Sentinel-1 data freely available. This work is based in part on data services provided by the OpenTopography Facility with support from the National Science Foundation under NSF Award Numbers 1948997, 1948994 and 1948857. JM and RD carried out part of this work with funding from NASA's Earth Surface and Interior program, Grant #80NSSC22K0464.

References

Bakun, W. H., Flores, C. H., & ten Brink, U. S. (2012). Significant Earthquakes on the Enriquillo fault system, Hispaniola, 1500–2010: Implications for seismic HazardSignificant Earthquakes on Enriquillo fault system, Hispaniola, 1500–2010: Implications for hazard. *Bulletin of the Seismological Society of America*, *102*(1), 18–30. https://doi.org/10.1785/0120110077

Bekaert, D. P. S., Walters, R. J., Wright, T. J., Hooper, A. J., & Parker, D. J. (2015). Statistical comparison of InSAR tropospheric correction techniques. *Remote Sensing of Environment*, *170*, 40–47. https://doi.org/10.1016/j.rse.2015.08.035

Benford, B., DeMets, C., & Calais, E. (2012). GPS estimates of microplate motions, northern Caribbean: Evidence for a Hispaniola microplate and implications for earthquake hazard. *Geophysical Journal International*, *191*(2), 481–490. https://doi.org/10.1111/j.1365-246x.2012.05662.x

Calais, É., Symithe, S., Mercier de Lépinay, B., & Prépetit, C. (2016). Plate boundary segmentation in the northeastern Caribbean from geodetic measurements and Neogene geological observations. *Comptes Rendus Geoscience*, *348*(1), 42–51. https://doi.org/10.1016/j.crte.2015.10.007

Calais, E., Symithe, S., Monfret, T., Delouis, B., Lomax, A., Courboulex, F., et al. (2022). Citizen seismology helps decipher the 2021 Haiti earthquake. *Science*, *376*(6590), 283–287. https://doi.org/10.1126/science.abn1045

Chen, C. W., & Zebker, H. A. (2001). Two-dimensional phase unwrapping with use of statistical models for cost functions in nonlinear optimization. *Journal of the Optical Society of America A*, *18*(2), 338–351. https://doi.org/10.1364/josaa.18.000338

Chen, C. W., & Zebker, H. A. (2002). Phase unwrapping for large SAR interferograms: Statistical segmentation and generalized network models. *IEEE Transactions on Geoscience and Remote Sensing*, *40*(8), 1709–1719. https://doi.org/10.1109/TGRS.2002.802453

Conrad, E. M., Faccenna, C., Stockli, D. F., & Becker, T. (2020). Cenozoic evolution of the Northern Caribbean plate boundary: Insights from thermochronomentric, kinematic and geomorphic data (Vol. *52*). . [Poster presentation]. Geological Society of America, USA, 52. https://doi.org/10.1130/abs/2020AM-353996

Corbeau, J., Rolandone, F., Leroy, S., Mercier de Lépinay, B., Meyer, B., Ellouz-Zimmermann, N., & Momplaisir, R. (2016). The northern Caribbean plate boundary in the Jamaica Passage: Structure and seismic stratigraphy. *Tectonophysics*, *675*, 209–226. https://doi.org/10.1016/j.tecto.2016.03.022

Corbeau, J., Rolandone, F., Leroy, S., Meyer, B., Mercier de Lépinay, B., Ellouz-Zimmermann, N., & Momplaisir, R. (2016). How transpressive is the northern Caribbean plate boundary? *Tectonics*, *35*(4), 1032–1046. https://doi.org/10.1002/2015tc003996

DeMets, C., Gordon, R. G., & Argus, D. F. (2010). Geologically current plate motions. *Geophysical Journal International*, *181*(1), 1–80. https://doi.org/10.1111/j.1365-246x.2009.04491.x

DeMets, C., & Wiggins-Grandison, M. (2007). Deformation of Jamaica and motion of the Gonave microplate from GPS and seismic data. *Geophysical Journal International*, *168*(1), 362–378. https://doi.org/10.1111/j.1365-246x.2006.03236.x

Doin, M.-P., Lasserre, C., Peltzer, G., Cavalié, O., & Doubre, C. (2009). Corrections of stratified tropospheric delays in SAR interferometry: Validation with global atmospheric models. *Journal of Applied Geophysics*, *69*(1), 35–50. https://doi.org/10.1016/j.jappgeo.2009.03.010

Douilly, R., Haase, J. S., Ellsworth, W. L., Bouin, M., Calais, E., Symithe, S. J., et al. (2013). Crustal structure and fault geometry of the 2010 Haiti Earthquake from temporary seismometer deployments. *Bulletin of the Seismological Society of America*, *103*(4), 2305–2325. https://doi.org/10.1785/0120120303

Dziewonski, A. M., Chou, T.-A., & Woodhouse, J. H. (1981). Determination of earthquake source parameters from waveform data for studies of global and regional seismicity. *Journal of Geophysical Research*, *86*(B4), 2825–2852. https://doi.org/10.1029/JB086iB04p02825

Ekström, G., Nettles, M., & Dziewonski, A. M. (2012). The global CMT project 2004-2010: Centroid-moment tensors for 13, 017 earthquakes. *Physics of the Earth and Planetary Interiors*, *200–201*, 1–9. https://doi.org/10.1016/j.pepi.2012.04.002

Farr, T. G., Rosen, P. A., Caro, E., Crippen, R., Duren, R., Hensley, S., et al. (2007). The Shuttle radar topography mission. *Reviews of Geophysics*, *45*(2), RG2004. https://doi.org/10.1029/2005rg000183

Fattahi, H., Agram, P., & Simons, M. (2017). A network-based enhanced spectral diversity approach for TOPS time-series analysis. *IEEE Transactions on Geoscience and Remote Sensing*, *55*(2), 777–786. https://doi.org/10.1109/tgrs.2016.2614925

French, C. D., & Schenk, C. J. (2004). *Map showing geology, oil and gas fields, and geologic provinces of the Caribbean region*. U.S. Geological Survey Open-File Report. 97-470-K. https://doi.org/10.3133/ofr97470K

Goldstein, R. M., & Werner, C. L. (1998). Radar interferogram filtering for geophysical applications. *Geophysical Research Letters*, *25*(21), 4035–4038. https://doi.org/10.1029/1998gl900033

Jolivet, R., Grandin, R., Lasserre, C., Doin, M.-P., & Peltzer, G. (2011). Systematic InSAR tropospheric phase delay corrections from global meteorological reanalysis data. *Geophysical Research Letters*, *38*(17). https://doi.org/10.1029/2011gl048757

Jónsson, S., Zebker, H., Segall, P., & Amelung, F. (2002). Fault slip distribution of the 1999 M w 7.1 Hector Mine, California, earthquake, estimated from satellite radar and GPS measurements. *Bulletin of the Seismological Society of America*, *92*(4), 1377–1389. https://doi.org/10.1785/0120000922

Leroy, S., Ellouz-Zimmermann, N., Corbeau, J., Rolandone, F., deLepinay, B. M., Meyer, B., et al. (2015). Segmentation and kinematics of the North America-Caribbean plate boundary offshore Hispaniola. *Terra Nova*, *27*(6), 467–478. https://doi.org/10.1111/ter.12181

Mann, P., Calais, E., Ruegg, J.-C., DeMets, C., Jansma, P. E., & Mattioli, G. S. (2002). Oblique collision in the northeastern Caribbean from GPS measurements and geological observations. *Tectonics*, *21*(6), 7–26. https://doi.org/10.1029/2001tc001304

Mann, P., Taylor, F. W., Edwards, R. L., & Ku, T. L. (1995). Actively evolving microplate formation by oblique collision and sideways motion along strike-slip faults: An example from the northeastern Caribbean plate margin. *Tectonophysics*, *246*(1–3), 1–69. https://doi.org/10.1016/0040-1951(94)00268-E

Maurer, J. (2022). *2021 Haiti Earthquake*. https://doi.org/10.17605/OSF.IO/F8W9E

Maurer, J., & Vernon, A. (2022). *Updated and expanded CCAF-DB (version 1.0)* [Computer software]. https://doi.org/10.5281/zenodo.6324242

McTigue, D. F., & Segall, P. (1988). Displacements and tilts from dip-slip faults and magma chambers beneath irregular surface topography. *Geophysical Research Letters*, *15*(6), 601–604. https://doi.org/10.1029/GL015i006p00601

Okada, Y. (1985). Surface deformation due to shear and tensile faults in a half-space. *Bulletin of the Seismological Society of America*, *75*(4), 1135–1154. https://doi.org/10.1785/bssa0750041135

Okuwaki, R., & Fan, W. (2022). Oblique convergence causes both thrust and strike-slip ruptures during the 2021 M 7.2 Haiti Earthquake. *Geophysical Research Letters*, *49*(2), e2021GL096373. https://doi.org/10.1029/2021gl096373

Possee, D., Keir, D., Harmon, N., Rychert, C., Rolandone, F., Leroy, S., et al. (2019). The tectonics and active faulting of Haiti from seismicity and tomography. *Tectonics*, *38*(3), 1138–1155. https://doi.org/10.1029/2018tc005364

Prentice, C. S., Mann, P., Crone, A. J., Gold, R. D., Hudnut, K. W., Briggs, R. W., et al. (2010). Seismic hazard of the Enriquillo–Plantain Garden fault in Haiti inferred from palaeoseismology. *Nature Geoscience*, *3*(11), 789–793. https://doi.org/10.1038/ngeo991

Ragon, T., Sladen, A., Bletery, Q., Vergnolle, M., Cavalié, O., Avallone, A., et al. (2019). Joint inversion of coseismic and Early postseismic slip to optimize the information content in geodetic data: Application to the 2009 Mw6.3 L'aquila Earthquake, Central Italy. *Journal of Geophysical Research: Solid Earth*, *124*(10), 10522–10543. https://doi.org/10.1029/2018JB017053

Rosen, P. A., Gurrola, E., Sacco, G. F., & Zebker, H. (2012). The InSAR scientific computing environment. In *EUSAR 2012; 9th European conference on synthetic aperture radar* (pp. 730–733).

Saint Fleur, N., Feuillet, N., Grandin, R., Jacques, E., Weil-Accardo, J., & Klinger, Y. (2015). Seismotectonics of southern Haiti: A new faulting model for the 12 January 2010 M7.0 earthquake. *Geophysical Research Letters*, *42*(23). https://doi.org/10.1002/2015GL065505

Saint Fleur, N., Klinger, Y., & Feuillet, N. (2020). Detailed map, displacement, paleoseismology, and segmentation of the Enriquillo-Plantain Garden Fault in Haiti. *Tectonophysics*, *778*, 228368. https://doi.org/10.1016/j.tecto.2020.228368

Styron, R., García-Pelaez, J., & Pagani, M. (2020). CCAF-DB: The Caribbean and Central American active fault database. *Natural Hazards and Earth System Sciences*, *20*(3), 831–857. https://doi.org/10.5194/nhess-20-831-2020

Symithe, S., & Calais, E. (2016). Present-day shortening in Southern Haiti from GPS measurements and implications for seismic hazard. *Tectonophysics*, *679*, 117–124. https://doi.org/10.1016/j.tecto.2016.04.034

Symithe, S., Calais, E., De Chabalier, J. B., Robertson, R., & Higgins, M. (2015). Current block motions and strain accumulation on active faults in the Caribbean. *Journal of Geophysical Research: Solid Earth*, *120*(5), 3748–3774. https://doi.org/10.1002/2014JB011779

Symithe, S. J., Calais, E., Haase, J. S., Freed, A. M., & Douilly, R. (2013). Coseismic slip distribution of the 2010 M 7.0 Haiti Earthquake and resulting stress Changes on regional FaultsCoseismic slip distribution of the 2010 M 7.0 Haiti Earthquake. *Bulletin of the Seismological Society of America*, *103*(4), 2326–2343. https://doi.org/10.1785/0120120306

Uieda, L., Tian, D., Leong, W. J., Jones, M., Schlitzer, W., Toney, L., et al. (2021). *PyGMT: A Python interface for the generic mapping tools*. https://doi.org/10.5281/ZENODO.5607255

UN Office for the Coordination of Humanitarian Affairs (UN-OCHA). (2021). *Haiti: Earthquake situation report no. 8 - final (29 November 2021)*. ReliefWeb. Retrieved from https://reliefweb.int/report/haiti/haiti-earthquake-situation-report-no-8-final-29-november-2021

Wang, K., & Fialko, Y. (2018). Observations and modeling of coseismic and postseismic deformation due to the 2015 Mw 7.8 Gorkha (Nepal) Earthquake. *Journal of Geophysical Research: Solid Earth*, *123*(1), 761–779. https://doi.org/10.1002/2017jb014620

Wimpenny, S., Copley, A., & Ingleby, T. (2017). Fault mechanics and post-seismic deformation at Bam, SE Iran. *Geophysical Journal International*, *209*(2), 1018–1035. https://doi.org/10.1093/gji/ggx065